Plasmonic Nanopillar Arrays for Large-Area, High-Enhancement Surface-Enhanced Raman Scattering Sensors

10 AUTHORS, INCLUDING:

Joshua David Caldwell
United States Naval Research Laboratory
147 PUBLICATIONS **1,072** CITATIONS

SEE PROFILE

R. W. Rendell
United States Naval Research Laboratory
127 PUBLICATIONS **2,709** CITATIONS

SEE PROFILE

Maraizu Ukaegbu
Western Washington University
8 PUBLICATIONS **126** CITATIONS

SEE PROFILE

Richard Kasica
National Institute of Standards and Technol…
45 PUBLICATIONS **343** CITATIONS

SEE PROFILE

Plasmonic Nanopillar Arrays for Large-Area, High-Enhancement Surface-Enhanced Raman Scattering Sensors

Joshua D. Caldwell,[†,*] Orest Glembocki,[†] Francisco J. Bezares,[†] Nabil D. Bassim,[†] Ronald W. Rendell,[†] Mariya Feygelson,[†] Maraizu Ukaegbu,[‡] Richard Kasica,[§] Loretta Shirey,[†] and Charles Hosten[‡]

[†]U.S. Naval Research Laboratory, 4555 Overlook Avenue, S.W., Washington, D.C. 20375, United States, [‡]Chemistry Department, Howard University, Washington, D.C. 20059, United States, and [§]Center for Nanoscale Science and Technology, National Institute for Standards and Technology, Gaithersburg, Maryland 20899, United States

Significant effort has been directed toward both understanding the mechanism of surface-enhanced Raman scattering (SERS) and to exploit its benefits for use in obtaining the largest Raman enhancement factors (G) possible, with single molecule detection having been reported from nm-sized, localized hot-spots and from tip enhanced Raman scattering.[1−3] However, in the case of a real world sensor, the detection of low levels of species is directly related to the probability of a molecule interacting with the active area of the sensor surface. The use of highly localized hot spots in this case relegates a large portion of the sensing area as inactive for detection. Therefore, as schemes for detecting chemical or biological species are anticipated to involve measuring large-areas at a given time (several micrometers to millimeters for instance), it can be expected that the average enhancement factor $\langle G \rangle$ over the entire array is more pertinent than the peak enhancement, G_{peak}. In addition, the best performance will not just require large $\langle G \rangle$, but will also require the smallest variability in G over the detection area. Therefore, as most SERS templates focus primarily on small collections of plasmonically coupled particles that are widely spaced from one another, not only will the $\langle G \rangle$ be significantly reduced with respect to G_{peak}, but also the variability between different positions on the samples will be quite large. Thus, fabrication of nanostructures with evenly distributed plasmonic fields featuring high $\langle G \rangle$ are desired, even at the cost of a reduction in G_{peak}.

Several studies have been undertaken investigating the surface plasmon resonance (SPR) from various periodic and aperiodic structures of Ag and/or Au nanoparticles both theoretically[4−6] and experimentally;[7−10]

ABSTRACT Efforts to create reproducible surface-enhanced Raman scattering (SERS)-based chemical and biological sensors has been hindered by difficulties in fabricating large-area SERS-active substrates with a uniform, reproducible SERS response that still provides sufficient enhancement for easy detection. Here we report on periodic arrays of Au-capped, vertically aligned silicon nanopillars that are embedded in a Au plane upon a Si substrate. We illustrate that these arrays are ideal for use as SERS sensor templates, in that they provide large, uniform *and* reproducible average enhancement factors up to $\sim 1.2 \times 10^8$ over the structure surface area. We discuss the impact of the overall geometry of the structures upon the SERS response at 532, 633, and 785 nm incident laser wavelengths. Calculations of the electromagnetic field distributions and intensities within such structures were performed and both the wavelength dependence of the predicted SERS response and the field distribution within the nanopillar structure are discussed and support the experimental results we report.

KEYWORDS: surface enhanced Raman scattering · SERS · electron-beam lithography · reactive ion etching · plasmonics · nanoparticles · plasmonic arrays · grating

however, few reports have focused on how such structures perform for SERS-based sensing applications. Those studies that did investigate the SERS behavior typically have focused on optimizing the G_{peak} observed within the nm-sized hot-spots between nanoparticles,[11] reporting very large G_{peak} values by considering only the spatial regions where the plasmonic fields persist, rather than the entire irradiated area. A discussion of the importance of exploring the benefits of large-area, uniform $\langle G \rangle$ has been reported by Genov et al.,[4] where the authors presented a numerical calculation and an analytical model of the predicted SERS enhancement from periodic arrays of Ag and Au nanospheres and cylindrical oblate disks with high aspect ratios, reporting that $\langle G \rangle$ values up to 2×10^{11} and 5×10^{10} are feasible within such structures, respectively. By comparison, Gopinath, et al.,[8] have recently reported experimental $\langle G \rangle = 3 \times 10^7$ in aperiodic arrays of tightly spaced Au nanostructures, while Yu, et al.[12,13] have

* Address correspondence to
joshua.caldwell@nrl.navy.mil.
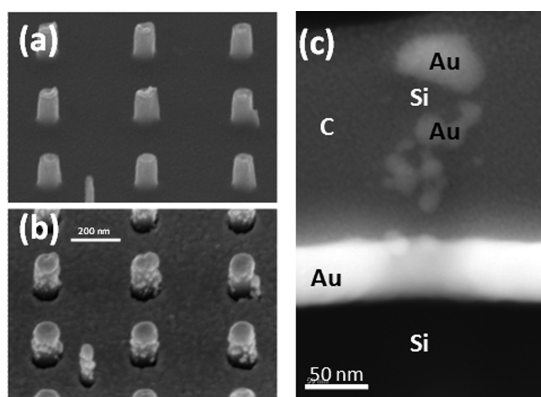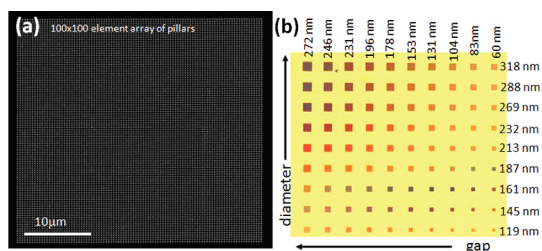
Figure 1. SEM micrographs of Si nanopillars collected at a 45 degree tilt (a) prior to and (b) following the deposition of 50 nm of Au *via* electron beam evaporation. (c) TEM micrograph of a single Au-coated Si nanopillar.

Figure 2. (a) A top-view SEM micrograph of a 100 × 100 nanopillar array. (b) An optical micrograph of the array pattern layout. Each colored square is an individual 100 × 100 nanopillar array. The dimensions listed correspond to the nanopillar diameter and interpillar gap associated with each array in the series prior to metal deposition as determined from SEM images.

reported enhancement factors from periodic Au nanohole and nanodisk arrays that were fabricated by ebeam lithography, reporting $\langle G \rangle = 4.2 \times 10^5$ and 1.3×10^3 for nanohole and nanodisk arrays, respectively. This is also consistent with the results from Baumberg *et al.*[7] where periodic arrays of nanohole were observed to provide $\langle G \rangle = 3 \times 10^6$. Thus, clearly the high theoretical values that Genov *et al.*[4] reported have not been attained experimentally. This discrepancy is due in part to the fact that in experimental situations, nanoparticles are either placed within a matrix or are fabricated onto the surface of a substrate. In either case, the substrate will have a significant impact on the plasmonic response of the nanoparticles,[14,15] even in an arrayed format.

Here we report on the SERS response from two-dimensional arrays of registered Au-capped, Si nanopillars embedded in a periodic Au-nanohole array located at the base of the nanopillars. The introduction of periodicity within these arrays has an important impact on $\langle G \rangle$, in that local variations in the electric fields associated with fabrication imperfections are averaged over the entire structure, and therefore their direct impact is minimized. The use of the combination of the nanodisks with the nanoholes in the Au film are found to also lead to an additional enhancement of the local fields. We previously reported that the combination of the localized plasmon modes within the nanodisks and the propagating plasmon modes in the nanohole array is required to attain high and uniform SERS enhancements.[16] Contrary to the inverted size dependence described by Yu *et al.*,[13] we found that the SERS response of a self-assembled monolayer of thiophenol on such nanostructures peaked at a specific diameter. Further, this diameter was found to be dependent upon the incident wavelength, with the strongest SERS response being observed at 785 nm excitation. The SERS intensity was also found to increase monotonically with increasing interpillar gap within the range of 85−298 nm for measurements at

both 785 and 633 nm incident. Overall, we report $\langle G \rangle$ up to 1.2×10^8 and 3.3×10^6 at 785 and 633 nm excitation, respectively. Recently, Li *et al.*[17] reported similarly large enhancements to those reported here using Au-coated SiO_2 arrays that were similar in structure to those reported by Chen and Jiang,[9] with the peak response being observed near 633 nm incident for SERS and extinction, respectively, while the optimal response observed here is found at 785 nm incident. Simulations of the expected SERS response from the structures reported here were found to be qualitatively consistent with the experimental results, predicting both the wavelength and the general diameter dependence that was experimentally observed at those excitation conditions. The simulations also indicate that the peak plasmonic fields are distributed both around the Au cap located on top of the Si nanopillars as well as around the nanoholes, with the latter providing larger electromagnetic fields at the optimal excitation conditions. This illustrates once again that the combination of the registered nanohole and nanodisks within the architecture we discuss here is required to attain the large $\langle G \rangle$ we report, consistent with our previous observations.[16] It should also be noted that the dielectric constant of the nanopillar is also very important in determining both the magnitude of the enhancement and its wavelength (nanopillar diameter) dependence.

RESULTS AND DISCUSSION

Plasmonic nanostructures comprising 100 × 100 arrays of ~160 nm tall, Au-coated Si nanopillars were fabricated. The nanopillars were fabricated using a chromium hard mask created *via* ebeam lithography and reactive ion etching, with a SEM illustrating the uncoated nanopillar structures presented in Figure 1a. Following nanopillar fabrication, they were overcoated with a thin (~50 nm) film of Au *via* e-beam evaporation, resulting in a mushroom-shaped cap on top and a thin Au film at the base of the nanopillars as shown in Figure 1b. As evidenced by the TEM micrograph presented in Figure 1 c, in addition to the Au cap and base film, small Au

TABLE 1. Listing of the Nanopillar Diameters and Interpillar Gaps Prior to and Following Deposition of 50 nm Au *via* Electron Beam Evaporation

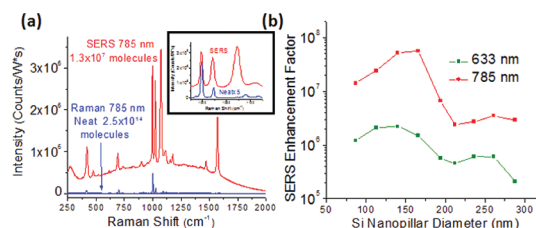| before metal deposition		after metal deposition	
diameter	interpillar gap	pillar cap diameter	interpillar cap gap
	86		60
87	109	119	83
113	130	145	104
140	157	161	131
166	180	187	153
194	204	213	178
212	222	232	196
236	257	269	231
261	272	288	246
288	298	318	272
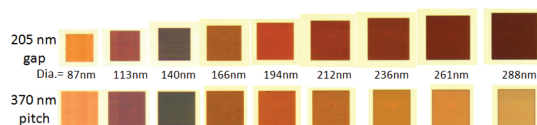
Figure 3. Optical micrographs of individual arrays as a function of diameter at (top row) constant 205 nm interpillar gap and (bottom row) constant 370 nm pitch. The images were collected at 50× magnification.

Figure 4. (a) Comparison of the SERS (optimal structure) and neat Raman spectra of benzene thiol collected at 785 nm incident. The number of molecules of benzene thiol that each measurement is probing is denoted in the figure. Inset: Zoomed in region of the spectra showing the three primary modes located near 1000 cm^{-1}, with the 998 cm^{-1} used for calculation of the SERS enhancement factor. Note that the neat spectra has been multiplied by a factor of 5 for easier direct comparison. (b) Diameter dependence of the SERS enhancement factor at a constant interpillar gap of 272 nm detected at 633 (green squares) and 785 (red circles) nm incident.

beads were also deposited onto the side-wall, with these beads falling within the range of 10−30 nm in diameter. For the large-area structures to be discussed here, an array of a 100 × 100 nanopillars were arranged into a cubic lattice. A SEM micrograph of such an array is presented in Figure 2a. To determine the role that the nanopillar diameter and interpillar gap played in the observed SERS intensity, a combinatorial approach was undertaken. As illustrated in the optical image presented in Figure 2b, 90 total arrays were fabricated, with each featuring a different nanopillar diameter and interpillar gap, with these parameters ranging from 85−298 nm, prior to Au deposition. A full outline of all of the diameters and gaps prior to and following Au deposition is provided in Table 1.

The optical and plasmonic responses of the arrays were studied using two techniques: optical reflection imaging and surface enhanced Raman scattering (SERS). The optical images allow us to see overall color changes associated with both the plasmonic and diffraction responses from these nanopillar arrays, while SERS measurements of a stable self-assembled monolayer (SAM) of benzene thiol enabled the measurement of the ⟨G⟩ from the various arrays.

Optical reflection images of each individual array were collected and compared as a function of diameter, interpillar gap, and array pitch. Presented in Figure 3 panels a and b are reflected white light images of a series of arrays with increasing nanopillar diameter at a constant interpillar gap and pitch,

respectively. For nanopillars with diameters smaller than 194 nm, large variations in the reflected color were observed with changing diameter, whereas those arrays featuring larger nanopillars exhibited minimal changes in the reflected color as the diameter was increased. This effect was observed when the arrays were compared at either constant gap (Figure 3a) or pitch (Figure 3b), thus indicating that the color changes observed at small diameters were dominated by changes in the surface plasmon resonance (SPR) condition, rather than being induced because of diffraction effects. This observation can be explained by the expected red-shift in the SPR condition with increasing nanoparticles size. For isolated disks, the SPR is dominated by the aspect ratio of the disk,[18,19] thus by increasing the diameter of a fixed height disk, the SPR will red-shift. For the small diameter structures, where the SPR condition is expected to occur within the visible portion of the electromagnetic spectrum, the observed color of the arrays would be primarily a function of the plasmon-induced absorption. As the diameter of the nanopillars is increased, the red-shift in the SPR would eventually push the SPR condition into the near-infrared (NIR), at which point, the plasmonic absorption would no longer influence the array color within the reflectance images. In all cases, as the array pitch (periodicity) approaches 300 nm, diffraction effects would be expected to become important and would therefore influence the observed color. From the images presented in Figure 3a,b, it would be anticipated that the SPR shifts into the NIR for structures with nanopillar diameters between 166 and 194 nm. Therefore, it should be anticipated that the peak in the SERS response detected at 785 nm incident light should be observed from arrays featuring nanopillars with diameters near the lower end of this range, whereas for 633 nm incident, the optimal performance should be observed at smaller diameters.

Presented in Figure 4a are Raman spectra that were collected from the nanopillar array exhibiting the highest SERS response (red) and from a neat spectra of thiophenol (blue) with both having been normalized to account for the acquisition time and laser power. The number of molecules contributing to the SERS response quoted within Figure 4a and used for determining $\langle G \rangle$, were calculated by taking into account the surface coverage of benzene thiol on the metal surface and the exposed Au surface area within the laser spot size, while the number of molecules contributing to the neat Raman spectra was calculated by taking into account the laser spot size and the collection volume. These calculations were used to determine the $\langle G \rangle$ for the various arrays, with full explanation $\langle G \rangle$ calculations being provided in the Methods section. Note that the SERS response is over an order of magnitude higher in intensity than the neat spectra, despite the fact that the SERS measurement sampled approximately 7 orders of magnitude less thiophenol molecules, as noted in the figure. In computing the SERS enhancements we used the intensity of the peak found at 998 cm^{-1}, which is due to a carbon−hydrogen wagging mode, and therefore is the furthest removed from the sulfur−gold bond, where modifications in the molecular polarizability and in turn the Raman intensity would be most dramatic. This peak was chosen to ensure that an accurate estimation of the enhancement factor could be established. The careful selection of the Raman mode used for the calculations of $\langle G \rangle$ is of the utmost importance, as the value of $\langle G \rangle$ will be artificially inflated if Raman modes from the C−C or C−S vibrations are used. For comparison, the three modes associated with vibrations about the aromatic ring are presented in the inset of Figure 4a, with these calculations of $\langle G \rangle$ based on the intensities of the modes at 998 (C−H wag), 1021 (C−C symmetric stretch) and 1071 (C−C asymmetric stretch)[20,21] cm^{-1} providing enhancement factors of 1.2×10^8, 3.8×10^8, and 1.4×10^9 at 785 nm incident for the optimal array structure. Additionally, choosing the strong Raman mode located at approximately 1571 cm^{-1}, which corresponds to a C−C symmetric stretch, leads to an enhancement factor of 2.7×10^9. However, while choosing the most appropriate peak is very important for calculating an accurate $\langle G \rangle$, the general trends within the diameter, gap, and pitch dependences were found to be relatively independent of the choice of Raman mode used for comparison. In Figure 4b we present the diameter dependence of the SERS enhancement factor for the 998 cm^{-1} mode as a function of diameter with a constant interpillar gap of 272 nm. The measurement of $\langle G \rangle$ was required not only for determining the efficiency of the arrays for use as SERS-based chemical sensors, but was also needed for a direct comparison to the theoretical calculations to be carried out.

Consistent with the expectations derived from the optical images presented in Figure 3, the diameter dependence presented in Figure 4b illustrates that the
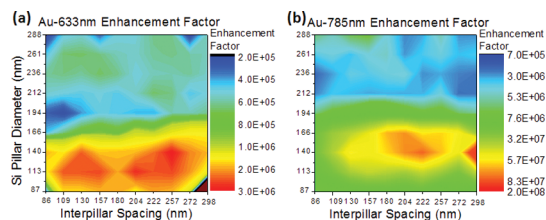
Figure 5. Contour plots of the SERS enhancement factor as a function of interpillar gap (*x*-axis) and Si nanopillar diameter (*y*-axis) collected using (a) 633 and (b) 785 nm incident excitation. The optimal diameter for SERS detection at each wavelength is identified by the center of the horizontal red region found in both plots. Note the different scales for the two contour plots.

optimal SERS response was detected from arrays with ∼150 nm nanopillars at 785 nm incident excitation. At 633 nm excitation the optimal response was observed to shift near 130 nm. As obtaining the peak SERS response requires that the center position of the SPR is near the incident and/or detected wavelengths, the peak SERS response at a shorter incident wavelength requires a blue-shift in the SPR peak. Such a shift would be induced by reducing the nanopillar diameter, which is consistent with the diameter dependence for the 785 and 633 nm SERS measurements reported. In addition to the primary peaks in the diameter dependences, a second, weaker peak was observed in the 250−270 nm range for both excitation conditions, with this peak being more predominant at the shorter wavelength measurements. It should be noted that the SERS measurements were also carried out using both 514 and 532 nm excitations, however, no clear SERS response was observed. In contrast to the strong dependence of the SERS response on the nanopillar diameter, only a slow monotonic increase in the SERS intensity was observed with increasing interpillar gap (not shown) for both excitation conditions. Similarly, a clear dependence of the SERS intensity on the array pitch was not discernible. A clearer presentation of the SERS response as a function of both nanopillar diameter and interpillar gap can be found in Figure 5, where contour plots of the $\langle G \rangle$ for each of the arrays using (a) 633 and (b) 785 nm excitation are presented. Again the strong dependence of the SERS intensity, and in turn $\langle G \rangle$, upon the nanopillar diameter in both cases is clear. Overall, large values for $\langle G \rangle$ were observed, with peak enhancements approaching 3.0×10^6 and 1.2×10^8 at 633 and 785 nm excitation, respectively. It should be noted that even for nonoptimal structures large enhancement factors were still observed, with the minimum values for the arrays studied at 633 and 785 nm only falling to 1.7×10^5 and 2.2×10^6, respectively, illustrating that while optimization of the structures can provide significant advantages in detection sensitivity, these structures provide significant response, even from nonoptimal architectures. Furthermore, spatial maps of the SERS intensity over specific arrays
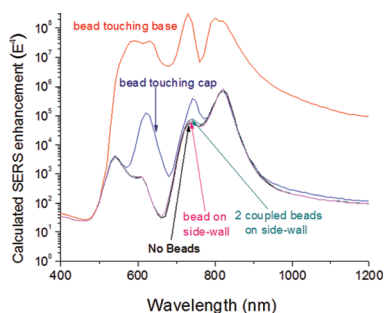
Figure 6. Spectral dependence of the SERS enhancement factor calculated using COMSOL Multiphysics under the quasi-static approximation for Au-coated, Si nanopillars with just the Au pillar cap and base film (no beads, black trace), and with Au beads located on the Si nanopillar sidewall either touching the base Au film (red trace), touching the Au cap (blue trace), located near the middle of the Si nanopillar (green trace, single bead; magenta trace, two coupled beads).

were also collected to determine the intra-array spatial variation in $\langle G \rangle$ and it was determined that such deviations were typically less than 30%, thus not only do these arrays provide very large enhancement factors, but they also offer high reproducibility and reliability, illustrating the promise of these structures for large-area SERS-based sensors for the detection of chemical and biological compounds. The enhancement factors reported here compare quite favorably with those reported for similar large-area structures.[7,8,12,13]

To gain a more complete understanding of the plasmonic field distributions from these Au-coated, Si nanopillar array structures, as well as to determine if simple modeling can provide predictive capabilities for such complex nanoarchitectures, finite-element simulations were undertaken using COMSOL Multiphysics under the quasi-static approximation. Arrays of nanopillars were modeled by constructing a single Si nanopillar placed on a square Si substrate. Both the top of the pillar and the Si substrate were covered with a 45 nm thick Au coating. The length and width of the Si substrate were chosen so that the pillar and substrate formed a unit cell within a periodic array. Periodic boundary conditions were then applied to the structure resulting in an infinite array with 100 nm interpillar gaps. Calculations using other gaps were also used, with minimal changes in the peak positions being observed provided the distance between the pillars was maintained at dimensions greater than 20 nm; thus, the simulations were carried out in a regime where interparticle plasmonic coupling was negligible. This observation is consistent with the monotonic increase in the SERS response observed as a function of interpillar gap.

From the TEM image presented in Figure 1c, it is observed that there are four major components of the individual nanopillars; (1) nanopillar cap, (2) hole array at the base, (3) metal beads on the sidewall and (4) cap-to-base gap. A good approximation of the mushroom

cap shape on top of the pillar was attained by creating a Au disk the width of the Si pillar and then adding a torroid with the same height of the disk, but overhanging the nanopillar edge by the 15 nm observed in the SEM and TEM images. This structure not only simulated the rounding of the edges, but also the higher radius of curvature of the cap with decreasing diameter. Simulations of the nanopillars with varying amounts of metal spheres (beads) on the side-walls at different spatial locations were performed in an effort to determine the role that the sidewall coverage played in the observed $\langle G \rangle$. The results of this study for a 150 nm Si pillar are presented in Figure 6. It was determined that when the beads were located away from the base or cap of the nanopillar that their impact upon $\langle G \rangle$ was minimal across the entire spectrum explored, independent of whether an isolated or two coupled beads were used. However, when the bead was placed near either the Au cap and/or the base film an SPR peak was induced near 633 nm, and in both cases led to an overall increase in $\langle G \rangle$ across the entire spectral range explored. It is important to note that no shifts in the peak positions of the SPR peaks were observed due to the inclusion of the sidewall coverage, with its introduction serving to enable the strong SERS response measured at 633 nm and provide an amplification of the response at 785 nm. From these calculations it is observed that the incorporation of beads on the sidewall near the pillar cap and/or base within the simulations are required in order to correctly simulate the relative SERS intensity of measurements carried out at 633 nm with respect to those using the 532 nm incident where no SERS response was found. However, while no SERS response at 532 nm was detected, the luminescence background caused the signal intensity to saturate the CCD detector at acquisition times longer than 20–30s. Therefore, it is possible that a weaker SERS response could have been observed if this luminescence could have been quenched or if the spectrometer featured a larger dynamic range. The important role that the sidewall coverage plays in enabling a SERS response at 633 nm was also observed in the study of Li et al.[17] on SiO_2 nanopillars, where the peak SERS response was observed at 633 and a significantly reduced response detected at 785 nm and calculations were performed using the finite difference time domain (FDTD) approach.

On the basis of a sampling of the TEM and SEM images of several nanopillars, it was determined that the best approximation of the nanopillar structure was one that included a bead located at both the cap and base, and three beads located near the center of the nanopillar side-wall. An image of the structure used for all simulations to be discussed going forward is presented in Figure 7a. SEM images were used to determine the nanopillar diameters and interpillar gaps prior to and following Au deposition in order to determine the width of the mushroom cap with
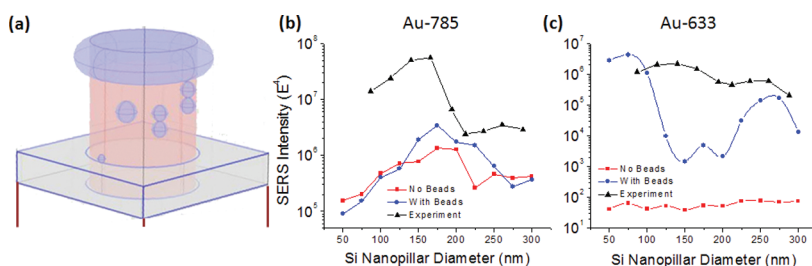
Figure 7. (a) Schematic of the nanopillar architecture used for the simulations presented in (b) and (c) as well as Figure 8. Diameter dependence of the SERS response calculated with (blue circles) and without (red squares) the Au beads on the sidewall in comparison to the corresponding experimental results (black triangles) at (b) 785 and (c) 633 nm incident.

respect to the nanopillar diameter. A summary of these measurements is provided in Table 1. In addition, the SEM images indicated that at the base of the pillar, there was a 5–10 nm gap between the edge of the nanopillar and the Au film. This gap was also found to play an important role in the calculated spectra and thus was also included in the final nanopillar structure to be simulated.

Using the nanopillar structure presented in Figure 7a, calculations to determine the ⟨G⟩ as a function of nanopillar diameter were carried out for direct comparison to the experimental results. The calculated ⟨G⟩ at 633 and 785 nm as a function of nanopillar diameter are presented in Figure 7b,c, respectively, both with (blue circles) and without (red squares) the beads on the nanopillar sidewalls, along with the corresponding experimental results (black triangles). In the case of the simulated spectra, the values reported correspond to the value of ⟨G⟩ at the average between the incident and detection wavelengths (820 and 670 nm for the 785 and 633 nm incident measurements). As these wavelengths represent the average spectral position between the incident and detected wavelengths, they are indicative of the SERS intensity from this detection scheme. It is important to note that similar results are achieved by averaging the SERS intensity at the incident and detection wavelengths. From these plots it is observed that good qualitative agreement in the general dependence line shape is obtained between the experimental and simulated results, both with and without beads, for the 785 nm excitation. Independent of the presence of the beads on the nanopillar sidewall, a peak in the diameter dependence is observed at approximately 175 nm, in good agreement with the experimental data. However, the experimental results exhibit an enhancement factor that is approximately 1.5 orders of magnitude higher than those predicted by the simulations. It is possible that this discrepancy is due to the chemical component of the total SERS enhancement that may account for up to 1–2 orders of magnitude.[22,23] For aromatic thiols, there is also a resonant Raman phenomenon that is due to the hybridized molecular orbital states created by the formation of the Au–S bond that is expected to also play some role in the observed SERS enhancement. These

states are the reason for the observed background fluorescence from benzene thiol, which as an unbound molecule does not fluoresce.[23] Such chemical and resonant effects can therefore account for the discrepancy between the calculations and the experimental results.

As implied by the ⟨G⟩ spectra presented in Figure 6, unlike the results at 785 nm, qualitative agreement between the simulations and experimental results was only attained at 633 nm incident when the beads were introduced onto the side wall. As is indicated in Figure 7c, the diameter dependence is essentially flat and very low in enhancement when the beads were absent, whereas the double-humped resonance found in the experimental results and the approximate enhancement amplitude were achieved only when the beads were included. While the actual spectral positions of the two peaks in the experimental and calculated ⟨G⟩ spectra are not completely coincident and the drop off in SERS intensity between 150 and 200 nm is over exaggerated by the simulations, the fact that the general line shape and approximate diameters at which the optimal ⟨G⟩ were observed were qualitatively similar between the experimental and calculated results despite the calculations being so heavily dependent upon the presence and location of the sidewall Au beads, is a testament to the high quality of the simulations and their predictive capabilities.

The observation that the SERS intensity passes through a maximum for a given incident wavelength at a specific nanoparticle diameter is consistent with most other observations reported in the literature.[8,17] Such an observation is also consistent with the wavelength shifts in the SPR condition known to occur with changing nanoparticle size. However, such results appear to contradict those reported by Yu et al.[13] In that study, the authors reported an inverted size dependence of the SERS response when comparing nanohole and nanodisk arrays with diameters and interparticle gaps similar to those discussed here. They observed a continual increase in ⟨G⟩ with increasing hole diameter, while the opposite was found for the nanodisk arrays. Thus, it would appear possible that the peak in the diameter dependence discussed here is the result of the overlapping of the inverted dependences
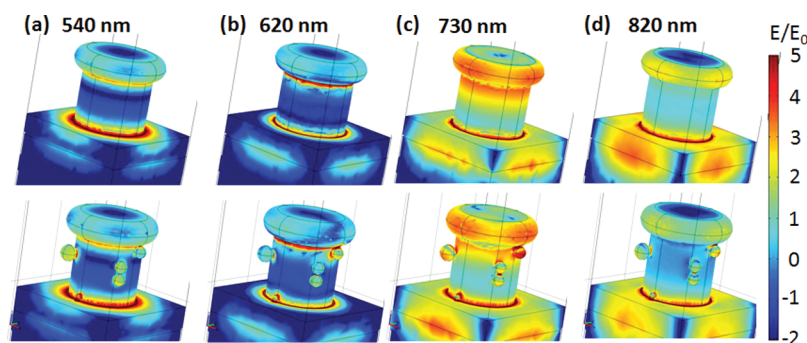
Figure 8. Contour plots of the calculated SERS enhancement across the surface of a 150 nm diameter Si nanopillar with 50 nm Au coverage measured at (a) 540, (b) 620, (c) 730, and (d) 820 nm, for nanopillars without (top row) and with (bottom row) Au beads on the Si nanopillar sidewall. The wavelengths chosen for the images presented correspond to the center position of the peaks observed in the spectra of these structures.

within our combined nanodisk and nanohole architecture and therefore would be consistent with the results of Yu et al.[12,13] However, recent work from our group determined that the overall diameter dependence remained unchanged upon the removal of the nanohole array film located at the base of the nanopillars, with only a reduction in the SERS intensity being induced.[16] It is possible that this discrepancy results from the presence of the continuous gold film that underlies both the nanodisk and nanohole arrays that those authors fabricated. While the impact of the underlying Au film in their structure is unclear, since it was directly in contact with the nanodisks, it can certainly be expected to aid in the delocalization of the plasmonic fields induced, thus reducing G, modifying the SPR of the subsequent geometries, and therefore the geometry required for attaining the optimal SERS response.[15] This comparison highlights the importance of understanding the role that each portion of the plasmonic architecture plays in providing the observed SERS enhancement. For instance, higher G values have been reported from nanohole[7,13] arrays in comparison to nanodisks,[8,12,13] indicating that the traveling plasmon modes that are present in nanohole arrays can provide significantly larger G values in comparison to the localized modes present in isolated nanoparticles such as nanodisks. This is consistent with the calculated plasmonic field distributions presented in Figure 8 (a–d), where such distributions are provided for 150 nm diameter nanopillars without (top) and with (bottom) beads on the sidewalls at 540, 620, 730, and 820 nm. The wavelengths chosen correspond to the four primary peaks observed in the ⟨G⟩ spectra presented in Figure 6. Here, large enhancements can be observed just under the pillar cap and in the gap between the nanopillar and the base film at the two lower wavelengths, whereas the fields begin to expand along the nanopillar wall, onto the cap overhang and along the Si sidewall as the wavelength is increased. It is the introduction of the enhanced SERS along the sidewalls and in the beads that lead to the large SERS response observed using a 633 nm incident excitation,

as indicated previously. By comparison, both the 785 nm incident and the 857 nm detection wavelengths reside on the peak in the G spectra located at 820 nm, where, as shown in Figure 8d, the plasmonic fields are primarily focused within the Au nanohole array and the gap between the nanopillar and base film. Therefore, consistent with the observations of Bezares et al.,[16] the collocation of both traveling and localized plasmon modes within the structures discussed here are the presumed reason for the large ⟨G⟩ observed.

CONCLUSIONS

Here we have reported on the SERS enhancement from a self-assembled monolayer of benzene thiol bound to Au-coated, silicon nanopillars embedded in a Au film (nanohole) that were arranged in periodic arrays, exploring the influence of nanopillar diameter and interpillar gap as well as the incident wavelength upon the detected SERS response. It was determined that a peak in the SERS intensity was found at approximately 130 and 150 nm for measurements carried out at 633 and 785 nm, respectively, with the corresponding average enhancement factors, ⟨G⟩ = 3.0×10^6 and 1.2×10^8 reported. A slow monotonic increase in the SERS intensity was observed as the interpillar gap was expanded from 85 to 298 nm, independent of nanopillar diameter, with no clear dependence upon array pitch (periodicity) having been observed. These latter effects indicate that while interference effects (diffraction) may play a role in the detected SERS response, this effect is minimal in comparison to the overwhelming influence of the nanopillar diameter, which controls the spectral position of the SPR and therefore the optimal SERS response. Simulations of G and its spatial distribution thoughout the nanopillar structure were undertaken using the quasi-static approximation. These calculations qualitatively predicted the behavior of the SERS enhancement as a function of diameter at both 633 and 785 nm, as well as the increasing SERS response observed with longer incident wavelength (532, 633, and 785 nm). The calculations illustrate the spatial distribution of the plasmonic

fields within the nanopillar architecture, thereby providing insight into the role of the various components of the structure in providing the SERS enhancements observed at each incident wavelength, and clearly identified the $\langle G \rangle$ at 633 nm as being the result of the presence of the Au beads located along the nanopillar sidewalls, in particular those located near the nanopillar cap and base. The $\langle G \rangle$ measured at 785 nm was found to be primarily dependent upon the plasmonic

fields located at the nanopillar base (hole array) and to some extent the nanopillar cap. These results indicate that the traveling plasmons located within the Au-film that is perforated by the nanopillars in the array play a significant role in determining the SERS enhancement factor and that the peak in $\langle G \rangle$ at a given diameter is a key feature of the plasmonic architectures, such as arrays of nanoholes, nanodisks, and combinations thereof.

METHODS

Nanopillar Array Fabrication. The silicon nanopillar arrays were fabricated on 4″ n-type Si wafers. Prior to processing, the native oxide was stripped in a 2% HF solution, rinsed in DI water, and then cleaned using the SC1 solution for 10 min before a final isopropyl alcohol (IPA) spray rinse and N_2 blow dry. Poly(methyl methacrylate) (PMMA) was spun onto the Si wafer for patterning (495 molecular weight, 3% dilution) at 4000 rpm for 35 s, followed by a 20 min vacuum bake at 140 °C. Periodic arrays of dots were written into the PMMA layer *via* a Vistec electron beam lithography system. The dot diameters ranged from 87 to 288 nm, while the gaps ranged from 85 to 298 nm and were arranged into a full-factorial arrangement of 100 × 100 dot arrays as shown in the optical reflectance image presented in Figure 2b. A planview SEM image of a 100 × 100 array of pillars is shown in Figure 1a, illustrating the square pattern, circularity, and uniformity in pitch of the dots. Following patterning, the resist was developed in 1:3 MIBK/IPA mixture for 60 s, and then spray rinsed with IPA and blown dry with dry nitrogen. A 30 nm thick film of chrome was deposited *via* e-beam evaporation at 1 Å/s, and the pattern of chrome dots was revealed *via* a standard lift off process in *n*-methylpyrolidone (nmp). The chrome dots were then used as a hard mask for reactive ion etching (RIE) of the Si substrate to form pillars, as shown in the SEM images collected at 45° tilt that are presented in Figure 1a, b. The RIE process was carried out in 12 sccm of CHF_3 and 16 sccm of SF_6 in a chamber held to a pressure of 18 mTorr, with an RF power of 140 W. This chemistry provided for an anisotropic etch that enabled the formation of the straight sidewalls of the nanopillars presented here. The 160 nm tall pillars were fabricated *via* a 10 min, 48 s etch. Once the pillars were formed, the chrome was removed *via* wet-chemical etching, and the now bare silicon pillars were imaged in the SEM to determine the pillar diameters and interpillar gaps of each array prior to the deposition of the metal overcoat. Following this, the nanopillars were coated with Au *via* e-beam evaporation. It was determined *via* SEM and TEM imaging that approximately 45 nm of Au was deposited on the pillar tops and the base substrate, with an approximate 5−10 nm gap between the edge of the Au base film and the Si nanopillar sidewall. The coverage on the pillar caps formed a mushroom cap shape, as shown in Figure 1b,c, with the caps extending an additional 12−15 nm beyond the width of the pillars. A summary of the nanopillar diameters and interpillar gaps before and after Au deposition is provided in Table 1. In all cases some discontinuous sidewall coverage was also created.

TEM Preparation and Imaging. An FEI Nova 600 dual-beam focused ion beam (FIB) tool was used to both image and prepare the cross-sectional TEM samples of the nanopillars. During FIB preparation, the electron beam in the dual-beam system was used to deposit a conformal protective nanocrystalline carbon layer in order to prevent sputtering of the gold off of the nanopillars during ion beam imaging and alignment. The TEM samples were evaluated in a JEOL 2200F microscope viewed in both high-resolution and scanning-TEM mode using a high-angle annular detector (HAADF) that provides contrast based on atomic mass. Several pillars were examined to provide basis measurements for the quasi-static calculations in COMSOL Multiphysics.

SERS Detection. To use the nanopillar arrays for surface-enhanced Raman scattering (SERS), the arrays were immersed in a 1×10^{-3} M solution of benzene thiol in ethanol for approximately 18 h to ensure that a complete SAM was formed on the nanopillar surface. SERS measurements were carried out using a DeltaNu ExamineR micro-Raman system using the 532, 633, and 785 nm incident laser lines of the various modules. A summary of the acquisition parameters for the various wavelengths and maximum and minimum enhancement factors are presented in Table 2. For each array and incident wavelength, several spectra were collected at various positions to ensure a reproducible SERS response was attained. Spatial mapping of the SERS intensity was carried out using the automated Prior stage mounted on the microscope. It was determined that the standard deviation in the SERS intensities were limited to approximately 30% within a given array. The SERS response at a given point was found to be highly reproducible, with variations in the detected response being limited to about 5%.

Enhancement Factor Calculations. To get an accurate approximation of the enhancement factor, the neat spectrum of benzene thiol was collected over 5 s using the liquid sample monitor included in the DeltaNu Examiner microscope at the various wavelengths. The powers used for these measurements were 3.6, 2.0, and 8.2 mW outputs of the 532, 633, and 785 nm incident laser lines, with a laser spot size of 30 μm and a depth of focus of 60 μm.

The enhancement factor G is defined as

$$G = \left(\frac{I^{SERS}/N^{SERS}}{I^{Raman}/N^{Raman}} \right) \quad (1.1)$$

where I^{SERS}, I^{Raman}, N^{SERS}, and N^{Raman} are the SERS and Raman intensities in counts and the number of probed molecules in the SERS and Raman measurements, respectively. For direct comparisons between the two measurements, corrections to the detected intensities must be made to compensate for the acquisition time and incident laser power. The corrected SERS intensity is therefore defined as

$$I^{SERS}_{Corr} = I^{SERS}/(tP) \quad (1.2)$$

where t and P are the acquisition time in seconds and laser power in Watts. The number of molecules probed *via* the SERS process may be written as follows:

$$N^{SERS} = \rho_{surf} N_A \frac{(A_{surf}/\text{unit-cell})}{(N^{pillar}/A_{spot})} \quad (1.3)$$

where ρ_{surf} is the surface coverage of benzene thiol on which has been reported as approximately 0.544 nmol/cm^2,[20,24−26] N_A = Avogadro's number, and A_{surf}/unit-cell is the SERS-active surface area of the nanopillar (Au cap, sidewall Au coverage, and Au base film) per unit cell (one nanopillar and the surrounding base film) and N^{pillar}/A_{spot} represents the number of nanopillars within the area of the laser spot-size. The surface area per unit cell may be defined as follows:

$$A_{surf}/\text{unit-cell} = (2\pi r_{Au}^2 + 2\pi r_{Au} d_{Au}) + [(2r_{Si} + s_{Si})^2 - \pi r_{Si}^2] \quad (1.4)$$

TABLE 2. Listing of the Relevant Acquisition Parameters for the Sers Measurements Carried out at the Three Primary Incident Wavelengths Explored. The Maximum and Minimum Enhancement Factors Observed at Each Wavelength Are Also Reported

incident wavelength (nm)	spot size (μm)	acquisition time (s)	laser power (mW)	Max EF	Min EF
532	2	1—30	3.2	0	0
633	2	10	2.0	3.0×10^6	1.7×10^5
785	2	2	8.2	1.2×10^8	2.2×10^6

where r_{Au} and r_{Si} are the radius of Au cap and Si nanopillar, respectively, s_{Si} is the interpillar gap between adjacent Si nanopillars, and d_{Au} is the thickness of Au cap on top of the pillars. In this case, the first term represents the surface area of the pillar cap, while the second term defines the surface area of the surrounding perforated Au film minus the missing hole where the nanopillar is embedded. In this calculation, the surface area of the exposed Si pillar was neglected as the plasmonic fields highest at or near the Au nanostructures, as indicated in the simulated plasmonic field distributions presented in Figure 8 (a—d); however, it is important to note that its inclusion did not significantly modify the reported $\langle G \rangle$.

The number of nanopillars located within the laser spot size used in the measurements is defined as follows:

$$N^{pillar}/A_{spot} = \frac{A_{spot}}{A_{unit-cell}} \quad (1.5)$$

where $A_{spot} = \pi r_{spot}^2$ and $A_{unit-cell} = (2r_{Si} + s_{Si})^2$.

To finish the comparison, the bulk Raman intensity is normalized to account for the laser power and acquisition times used,

$$I_{Corr}^{Raman} = I_0^{Raman}/(tP) \quad (1.6)$$

and

$$N^{Raman} = \frac{\rho}{(MW \times V)}N_A \quad (1.7)$$

where $\rho = 1.073$ g/mL and MW = 110.18 g/mol are the density and molecular weight of benzene thiol and V is the collection volume of the liquid sample monitor, which can be defined as

$$V = \pi r_{spot}^2 d \quad (1.8)$$

where d is the collection depth.

Theoretical Considerations. The Raman scattering process depends on light scattered from molecular vibrations in a solid, liquid, or a gas. In SERS, the Raman scattering from molecules adsorbed on nanostructured metal substrates is significantly increased by the strong optical fields associated with the creation of surface plasmons. Theoretically, G for SERS depends upon the dielectric properties of the molecule and the geometry and dielectric properties of the metal nanostructure. Therefore, G can be written as follows:

$$G(r_m, \omega) = \left| \frac{E_{total}(r_m, \omega)}{E_0(\omega)} \right|^4 \quad (1.9)$$

where $E_0(\omega)$ is the incident electric field and $E_{total}(r_m, \omega)$ is the total field at the location of the molecule, r_m. It is important to note that the total electric field is a vector quantity and that it contains contributions from the incident field, as well as the electric field induced by the excitation of the surface plasmons when they are in the presence of this incident field. Hence, the observed SERS enhancement is expected to be proportional to the electric field intensity to the fourth power. Equation 1.9 has an analytical form for the case of solid spheres and cylinders, however, more complex geometries or interacting nanoparticles must be treated with a numerical solution of Maxwell's equations. The quasistatic approximation to Maxwell's equations is appropriate when the geometries of the scattering aggregates are much smaller than the wavelength of the incident light and for nanoparticle arrays with periodicities below the diffraction limit ($\lambda/2$). Genov et al.[4] have shown

further that the ability of a quasistatic description of the field enhancements in periodic arrays is also governed primarily by the packing density parameter, given by γ = pillar diameter/interpillar gap, which determines the intensity of local field factors. Larger packing densities correspond to more localized EM resonances between the elements of the array and puts conditions closer to the quasistatic limit. They have demonstrated that nanoparticle arrays with $\gamma > 5$ can be quantitatively or semiquantitatively calculated under quasistatic conditions and such arrays are not sensitive to radiative losses due to retardation or damping effects.

Within the quasistatic limit, Maxwell's equations can be reduced to:

$$\nabla \cdot \{\sigma(\vec{r})[-\nabla\phi(\vec{r}) + E_0]\} = 0 \quad (1.10)$$

where σ is the local conductivity and ϕ is the local electric potential. To simulate the structures discussed in this paper, this equation was solved numerically using the COMSOL Multiphysics. The structure used for the simulations is presented in Figure 7a. The thickness of the Au film was defined to be the same as that of the Au cap, while the radius of the pillar caps were chosen to correspond to values 15 nm larger than the nanopillar diameter. In an effort to account for the array periodicity and interference effects, the nanopillars were centered within a box with periodic boundary conditions that included a 100 nm interpillar gap in addition to the nanopillar diameter. The experimental samples were composed of periodic arrays of Au-capped Si nanopillars with gaps between the individual elements that were greater than 85 nm. At these gaps, interparticle plasmonic coupling between the elements is negligibly small[11] and thus can be ignored. It is well-known that the quasistatic approximation is limited to geometries and periodicities less than the wavelength of light. Because the excitation lasers used in our experiments have wavelengths of 532, 633, and 785 nm, this corresponds to diameters less than 200 nm, with simulations of larger diameters potentially leading to an underestimation of the SERS enhancement. Furthermore, 100 nm interpillar gaps lead to packing densities in the quasistatic range $\gamma > 5$ for pillar diameters $d \geq 50$ nm. As a further check to ensure that the quasistatic approximation was appropriate, full-wave simulations that incorporated the time-dependent form of Maxwell's equations were also performed for a limited number of cases using the RF mode of the COMSOL program and produced qualitatively similar results.

REFERENCES AND NOTES

1. Jiang, J.; Bosnick, K.; Maillard, M.; Brus, L. Single Molecule Raman Spectroscopy at the Junctions of Large Ag Nanocrystals. *J. Phys. Chem. B* **2003,** *107*, 9964–9972.

2. Itoh, T.; Biju, V.; Ishikawa, M.; Kikkawa, Y.; Hashimoto, K.; Ikehata, A.; Ozaki, Y. Surface-Enhanced Resonance Raman Scattering and Background Light Emission Coupled With Plasmon of Single Ag Nanoaggregates. *J. Chem. Phys.* **2006,** *124*, 134708.

3. Maruyama, Y.; Futamata, M. Elastic Scattering and Emission Correlated with Single-Molecule SERS. *J. Raman Spectrosc.* **2005,** *36*, 581–592.

4. Genov, D. A.; Sarychev, A. K.; Shalaev, V. M.; Wei, A. Resonant Field Enhancements from Metal Nanoparticle Arrays. *Nano Lett.* **2004,** *4*, 153–158.

5. Huang, W.; Qian, W.; El-Sayed, M. A. The Optically Detected Coherent Lattice Oscillations in Silver and Gold Monolayer Periodic Nanoprism Arrays: The Effect of Interparticle Coupling. *J. Phys. Chem. B* **2005,** *109*, 18881–18888.

6. Kinnan, M. K.; Chumanov, G. Plasmon Coupling in Two-Dimensional Arrays of Silver Nanoparticles: II. Effect of the Particle Size and Interparticle Distance. *J. Phys. Chem. C* **2010,** *114*, 7496–7501.

7. Baumberg, J. J.; Kelf, T. A.; Sugawara, Y.; Cintra, S.; Abdelsalam, M. E.; Bartlett, P. N.; Russell, A. E. Angle-Resolved Surface-Enhanced Raman Scattering on Metallic Nanostructured Plasmonic Crystals. *Nano Lett.* **2005,** *5*, 2262–2267.

8. Gopinath, A.; Boriskina, S. V.; Premasiri, R.; Ziegler, L.; Reinhard, B. M.; Dal Negro, L. Plasmonic Nanogalaxies: Multiscale Aperiodic Arrays for Surface-Enhanced Raman Sensing. *Nano Lett.* **2009,** *9*, 3922–3929.

9. Chen, X.; Jiang, K. A Large-Area Hybrid Metallic Nanostructure Array and Its Optical Properties. *Nanotechnology* **2008,** *19*, 215305.

10. Wang, S.; Pile, D. F. P.; Sun, C.; Zhang, X. Nanopin Plasmonic Resonator Array and Its Optical Properties. *Nano Lett.* **2007,** *7*, 1076–1080.

11. Kottman, J. P.; Martin, O. J. F. Plasmon Resonant Coupling in Metallic Nanowires. *Opt. Express* **2001,** *8*, 655.

12. Yu, Q.; Braswell, S.; Christin, B.; Xu, J.; Wallace, P. M.; Gong, H.; Kaminsky, D. Surface-Enhanced Raman Scattering on Gold Quasi-3D Nanostructure and 2D Nanohole Arrays. *Nanotechnology* **2010,** *21*, 355301.

13. Yu, Q.; Guan, P.; Qin, D.; Golden, G.; Wallace, P. M. Inverted Size-Dependence of Surface-Enhanced Raman Scattering on Gold Nanohole and Nanodisk Arrays. *Nano Lett.* **2008,** *8*, 1923–1928.

14. Glembocki, O. J.; Rendell, R. W.; Alexson, D. A.; Prokes, S. M.; Mastro, M. A. Dielectric-Substrate-Induced Surface-Enhanced Raman Scattering. *Phys. Rev. B: Condens. Matter* **2009,** *80*, 085416.

15. Hill, R. T.; Mock, J. J.; Urzhumov, Y.; Sebba, D. S.; Oldenburg, S. J.; Chen, S.-Y.; Lazarides, A. A.; Chilkoti, A.; Smith, D. R. Leveraging Nanoscale Plasmonic Modes To Achieve Reproducible Enhancement of Light. *Nano Lett.* **2010,** *10*, 4150–4154.

16. Bezares, F. J.; Caldwell, J. D.; Glembocki, O. J.; Rendell, R. W.; Feygelson, M.; Ukaegbu, M.; Kasica, R.; Shirey, L.; Bassim, N. D.; Hosten, C. Probing Plasmonic Confinement: The Role of Propagating and Localized Surface Plasmons for SERS Enhancement in Periodic Nanostructures. *Plasmonics* **2011** submitted for publication.

17. Li, W.-D.; Ding, F.; Hu, J.; Chou, S. Y. Three-Dimensional Cavity Nanoantenna Coupled Plasmonic Nanodots for Ultrahigh and Uniform Surface-Enhanced Raman Scattering over Large Area. *Opt. Express* **2011,** *19*, 3925.

18. Kreibig, U.; Vollmer, M. *Optical Properties of Metal Clusters*; Springer-Verlag: New York, 1995.

19. Jensen, T. R.; Malinsky, M. D.; Haynes, C. L.; Van Duyne, R. P. Nanosphere Lithography: Tunable Localized Surface Plasmon Resonance Spectra of Silver Nanoparticles. *J. Phys. Chem. B* **2000,** *104*, 10549.

20. Carron, K. T.; Hurley, L. G. Axial and Azimuthal Angle Determination with Surface-Enhanced Raman Spectroscopy—Thiophenol on Copper, Silver and Gold Metal-Surfaces. *J. Phys. Chem.* **1991,** 95.

21. Li, S.; Wu, D.; Xu, X.; Gu, R. Theoretical and Experimental Studies on the Adsorption Behavior of Thiophenol on Gold Nanoparticles. *J. Raman Spectrosc.* **2007,** *38*, 1436–1443.

22. Moskovits, M. Surface-Enhanced Spectroscopy. *Rev. Mod. Phys.* **1985,** *57*, 783–826.

23. Alexson, D. A.; Badescu, S. C.; Glembocki, O. J.; Prokes, S. M.; Rendell, R. W. Metal—Adsorbate Hybridized Electronic States and Their Impact on Surface Enhanced Raman Scattering. *Chem. Phys. Lett.* **2009,** *477*, 144–149.

24. Taylor, C. E.; Pemberton, J. E.; Goodman, G. G.; Schoenfisch, M. H. Surface Enhancement Factors for Ag and Au Surfaces Relative to Pt Surfaces for Monolayers of Thiophenol. *Appl. Spectrosc.* **1999,** *53*, 1212–1221.

25. Gui, J. Y.; Stern, D. A.; Frank, D. G.; Lu, F.; Zapien, D. C.; Hubbard, A. T. Adsorption and Surface Structural Chemistry of Thiophenol, Benzyl Mercaptan and Alkyl Mercaptans—Comparative Studies at Ag(111) and Pt(111) Electrodes by Means of Auger Spectroscopy, Electron Energy Loss Spectroscopy, Low Energy Electron Diffraction and Electrochemistry. *Langmuir* **1991,** *7*, 955.

26. Stern, D. A.; Wellner, E.; Salaik, N.; Laguren-Davidson, L.; Lu, F.; Batina, N.; Frank, D. G.; Zapien, D. C.; Walton, N.; Hubbard, A. T. Adsorbed Thiophenol and Related-Compounds Studied at Pt(111) Electrodes by EELS, Auger Spectroscopy and Cyclic Voltammetry. *J. Am. Chem. Soc.* **1988,** *110*, 4887–4893.